Microstructural examination of oxide layers formed on an oxide dispersion strengthened ferritic steel exposed to supercritical water

Yun Chen [a,*], Kumar Sridharan [a], Todd R. Allen [a], Shigeharu Ukai [b]

[a] *Department of Engineering Physics, University of Wisconsin, 3335 Engineering Hall, 1415 Engineering Drive, Madison, WI 53706, United States*
[b] *Division of Materials Science and Engineering, Hokkaido University, Sapporo 060-8628, Japan*

Abstract

A transmission electron microscopy study was carried out on the oxide layers formed on a 9Cr oxide dispersion strengthened (ODS) ferritic steel after exposure to supercritical water at 500 °C with a 25 ppb dissolved oxygen concentration. Compared with the oxide layers formed on a conventional 9Cr steel NF616 ferritic steel with a similar major element composition and exposed to similar test conditions, the 9Cr ODS steel exhibited a different oxide structural morphology and growth mechanism. The most pronounced difference was the development of a substantially thick internal oxidation layer for the ODS steel that is associated with its finer grain size. For the oxidized ODS steel, yttrium and chromium rich oxide ribbons formed at the steel grain boundaries in the internal oxidation layer. The improved overall corrosion resistance of 9Cr ODS steel at elevated temperatures, as measured by weight gain data, may be a result of yttrium acting as a barrier for cation diffusion along oxide/metal grain boundaries. The gradual decrease in scale density with increasing exposure times appears to be caused by depletion of iron, which resulted in more vacancies and pores in the inner $(FeCr)_3O_4$ spinel layer.
© 2006 Elsevier B.V. All rights reserved.

PACS: 81.65.Mq; 64.75.+g; 66.30.−h; 68.37.Lp

1. Introduction

Heat-resistant alloys depend on the formation of a protective oxide layer on the alloy surface to minimize high temperature corrosion. Rare earth elements, such as yttrium added either elementally or as oxide dispersoids in alloys, have been shown to influence both oxide growth rate and adherence in Fe- and Ni-base alloys [1]. Our recent studies also indicate that a 9% Cr oxide dispersion strengthened (ODS) ferritic steel, where yttrium was present as Y–Ti–O dispersions, exhibited a lower oxide weight gain compared to other conventional non-ODS 9% Cr ferritic/martensitic steels when exposed to supercritical water at 500 °C and 25 MPa with a 25 ppb dissolved oxygen concentration [2]. It is generally

believed that the improved oxidation performance is caused by the modification of ionic transport due to the segregation of the rare earth elements to the oxide grain boundaries and to the oxide–metal interface [1,3–5], although some investigations reported no such segregation [6]. Similarly, many mechanisms have been proposed to explain the improved oxide scale adherence resulting from the addition of rare-earth elements. Notable among these are two models based on vacancy condensation [1,7] and relief of growth stress [6]. However, these mechanisms may be operational only in certain alloy systems and corrosion environments.

In the present study, we report the structural analysis of the oxide scale and the internal oxidation layer that formed on a 9Cr ODS ferritic steel during exposure to a supercritical water environment at 500 °C and 25 ppb dissolved oxygen.

2. Experimental

Bar stock of 9Cr ODS ferritic steel (24 mm diameter and 60 mm length) was supplied for this study by the Japan Atomic Energy Agency. The alloy had been annealed at 1050 °C for 60 min, air-cooled, and subsequently tempered at 800 °C for 60 min. The chemical composition of the steel is shown in Table 1. The details of the manufacturing process are described elsewhere [8]. Ferritic/martensitic steel NF616 which is a non-ODS steel but has major element compositions similar to the ODS steel was supplied by Nippon Steel Corporation and its chemical composition is also shown in Table 1.

The as received alloys were cut into test samples with dimensions of 31.8 mm × 12.7 mm × 0.5 mm, ground progressively with finer grit silicon-carbide paper, and then final polished with a 1 μm diamond paste. The corrosion experiments were performed in a natural circulation supercritical water corrosion loop at 500 °C and 25 MPa with a dissolved oxygen concentration of 25 ppb. The detailed construction and system capabilities of this supercritical water

loop have been described in a previous paper [9]. The exposure times were 333, 690, 1026 h.

After exposure, the extent of oxidation was evaluated by weight change measurement using a Scientech SA-80 Milligram Balance with an accuracy of 0.1 mg. A LEO 1530 field emission scanning electron microscope (SEM) equipped with energy dispersive spectroscopy (EDS) was used to examine oxide structure in both plan and cross-sectional views as well as to analyze composition across the oxide layer thickness. Transmission electron microscopy (TEM) cross-section samples of the oxidized regions were prepared by mechanical thinning, followed by argon ion milling to achieve electron transparency. A liquid-nitrogen cooled stage, a low ion-milling current/voltage, and a low sputtering angle were used to keep the sample cool during thinning, in order to minimize specimen damage. Electron diffraction, diffraction-contrast imaging, and high resolution TEM investigations were conducted in a CM200 transmission electron microscope operated at 200 kV.

3. Results

Fig. 1(a) and (b) shows the SEM cross-sectional morphology of the oxidize layers formed on 9Cr ODS ferritic steel after exposure for 1026 h, and corresponding composition versus depth profiles determined by EDS line-scans. Fig. 1(a) and (b) reveal that the oxidized thickness on 9Cr ODS consists of three different layers: an ∼9 μm outer iron oxide layer (between points labeled 1 and 2) which was identified to be magnetite, Fe_3O_4; an inner Fe/Cr-mixed oxide layer $(FeCr)_3O_4$ between points labeled 2 and 3 with ∼5 μm in thickness; and an innermost internal oxidation zone with a layer thickness of ∼5 μm between points labeled 3 and 4. In the internal oxidation layer, the oxygen concentration varied between 40 at.% and 20 at.%.

For comparison, the cross-sectional oxide morphology of the exposed 9Cr ferritic/martensitic steel NF616 and the corresponding EDS composition vs.

Table 1
Nominal chemical composition of 9Cr ODS steel and NF616 ferritic–martensitic steel investigated in this study (wt%, bal. Fe)

Alloy	C	Mn	P	S	Si	Ni	Cr	Mo	N	Al	W	Ti	V	Nb	Y	O
ODS[a]	0.14	0.05	<0.05	0.003	0.048	0.06	8.6	–	0.017	–	2	0.21	–	–	0.28	0.14
NF616	0.109	0.45	0.012	0.003	0.102	0.174	8.82	0.468	–	0.005	1.87	–	0.194	0.064	–	0.0042

[a] $[Y_2O_3] = 1.27 \times [Y] = 0.36$; $[Ex.O] = [Total\ O] - [O\ in\ Y_2O_3\ powder] = [O] - 0.27 \times [Y]$.
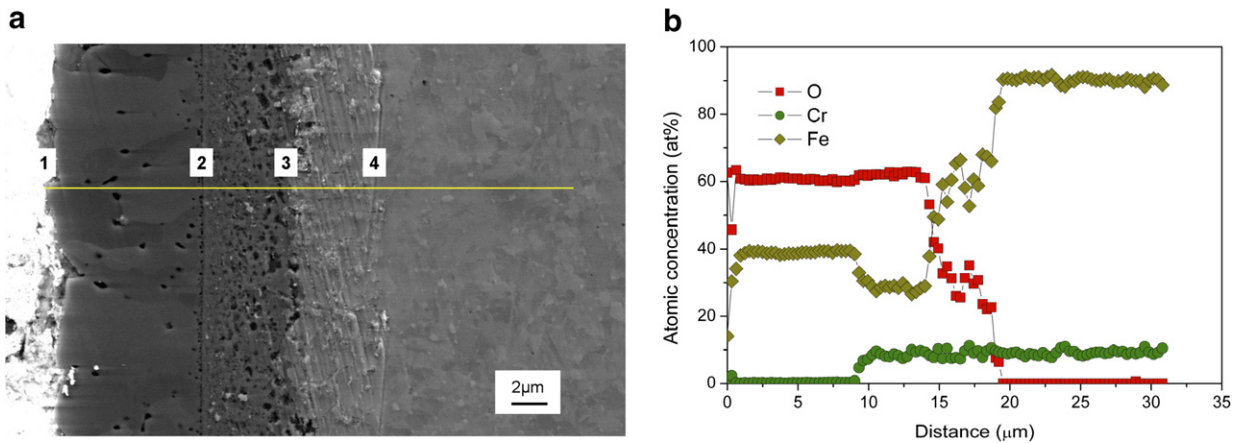
Fig. 1. (a) Cross-sectional SEM image of the 9Cr ODS ferritic steel after exposure to supercritical water at 500 °C for 1026 h and (b) corresponding composition profile across the oxide thickness.

depth profiles are shown in Fig. 2(a) and (b). The scale formed on the NF616 steel appears denser with less porosity than the one formed on the 9Cr ODS steel. There is no significant internal oxidation layer as may be noted in the SEM image shown in Fig. 2(a) and this is supported by the EDS line scans shown in Fig. 2(b), where a sharp decrease in O content is observed at the oxide layer/alloy interface. However, as in the case of the 9Cr ODS steel an outer Fe_3O_4 layer and an inner Fe/Cr-mixed oxide layer $(FeCr)_3O_4$ were observed. The thickness of the outer magnetite layer was ~11 μm (between points labeled 1 and 2 as marked in Fig. 2(a)) and that of the inner mixed layer was ~8.5 μm (between points labeled 2 and 3).

The weight gain as a function of oxide layer thickness for the 9Cr ODS and NF616 steels are presented in Fig. 3. Generally, the overall weight gain for the ODS steel was lower than the NF616 steel. Fig. 3 also indicates that the NF616 steel steadily gains oxygen and the linear proportionality between weight gain and thickness indicates that the density of the scale is relatively constant. On the other hand, the 9Cr ODS steel showed a weight gain that is not proportional to the film thickness. The scale density decreased gradually and, as shown in Fig. 1 tended to form a more porous structure at higher exposure times.

Fig. 4 shows the high resolution morphology of the Fe_3O_4 and $(FeCr)_3O_4$ layers formed on the
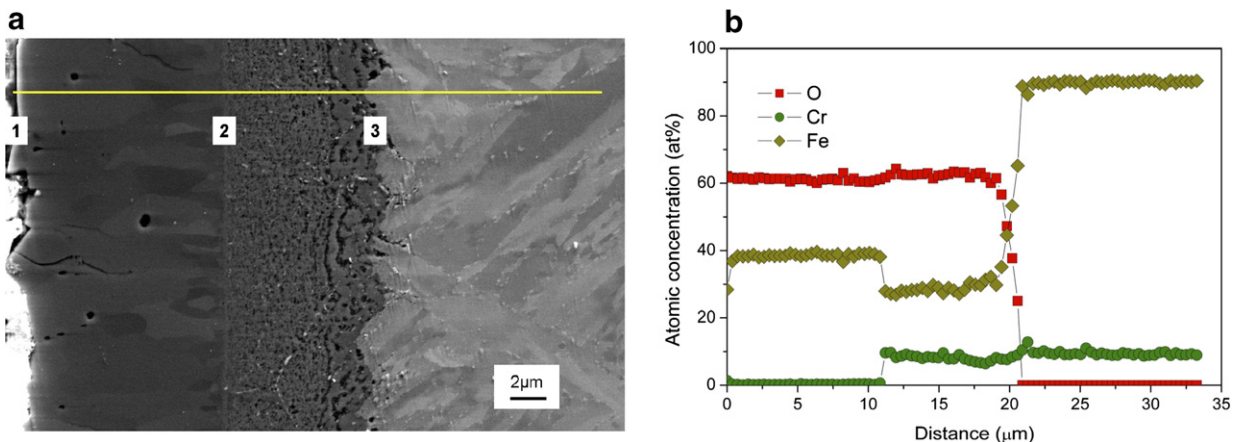

Fig. 2. (a) Cross-sectional SEM image of the 9Cr NF616 steel after exposure to supercritical water at 500 °C for 1026 h and (b) the corresponding composition profile across the oxide thickness.
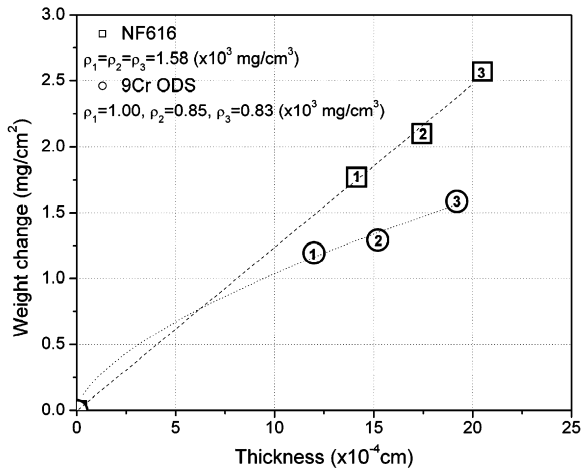
Fig. 3. Weight change (ΔW) as a function of oxide layer thickness (δ). Labels 1, 2 and 3 in represent the exposure times of 336 h, 690 h and 1026 h, respectively, and ρ indicates the apparent density of the oxide scale calculated by equation $\rho = \Delta W/\delta$.

9Cr ODS steel after exposure to supercritical water at 500 °C for 1026 h. The corresponding selected area electron diffraction pattern for the outer layer, shown in Fig. 5(a) was obtained by tilting the iron oxide grain to the [1 1 0] direction. The TEM micrograph (Fig. 4) clearly shows that the grains in the magnetite layer are a few microns in size and gener-
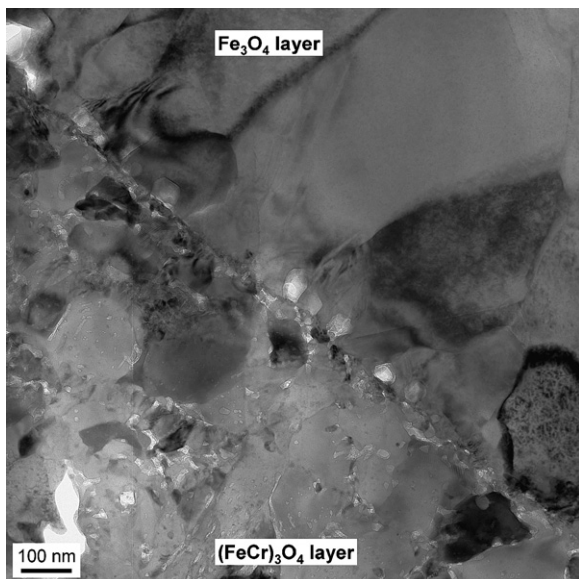

Fig. 4. TEM image showing the morphology of the magnetite and the spinel layers, and the interface between the two layers in the oxidized 9Cr ODS steel formed after exposure to supercritical water at 500 °C for 1026 h.

ally defect free. The grain boundaries are clear and free of secondary phases. Some pores are observed to form in the magnetite along the magnetite/spinel interface. This diffraction pattern for the magnetite layer is indicative of well-crystallized grains. The diffraction pattern for the inner $(FeCr)_3O_4$ region is composed of diffraction spots as well as rings as shown in Fig. 5(b). Randomly oriented grains exist in the spinel within 1 μm of the spinel/magnetite interface. High resolution electron microscopy (HREM) was employed to examine the grain boundary domain of this 1 μm region of the $(FeCr)_3O_4$ layer shows a HREM image of the domain marked by a square in which shows a general TEM image of this region. As shown in Fig. 6(a), an amorphous region was noted to be present in between the $(FeCr)_3O_4$ grains.

The representative microstructural morphology of the interior of the $(FeCr)_3O_4$ layer is shown in the TEM image in Fig. 7 along with the corresponding electron diffraction pattern. Most grains in this layer are approximately a few hundred nanometers in size. The grains contain sub-grains but the grain boundaries are difficult to discern. Diffraction rings presented in the inset image in Fig. 7 indicate that the grains are randomly oriented. As may be noted in Fig. 7, the structural morphology of the grains in the $(FeCr)_3O_4$ layer in the interior is different from that observed near $Fe_3O_4/(FeCr)_3O_4$ interface, the former being much more porous with pores preferentially distributed in the vicinity of the grain boundaries.

The morphology of a grain in the internal oxidation layer is shown in the TEM image in Fig. 8. The corresponding selected area electron diffraction patterns taken along the [0 1 1] zone axis of the ferritic phase is also presented in Fig. 8. Fig. 8(a) reveals that the grain is composed of three different components. The primary diffraction spots as marked by red color in Fig. 8(b) are clearly identified to be from the ferritic phase, originating from the base steel. Two different types of precipitates, on the size scale of a few nanometers are embedded within the ferritic matrix in Fig. 8. However, only one type of precipitates, which caused a large amount of Moiré fringes by overlapping themselves with the ferritic matrix, was identified to have cubic symmetry as shown in Fig. 8(b). The complex diffraction pattern in Fig. 8(b) allows us to calculate the lattice spacing d of the nanoprecipitates, using the diffractions from the ferritic matrix as an internal reference. The lattice parameter obtained from the diffraction
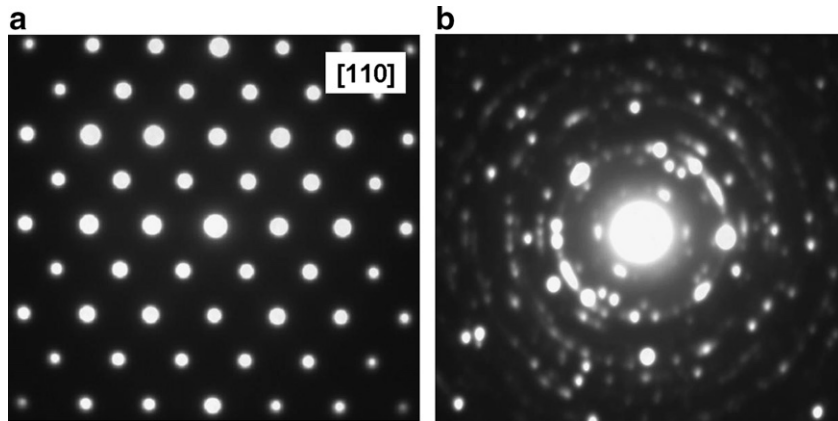
Fig. 5. Selected area electron diffraction patterns taken from (a) the outer Fe_3O_4 layer which aligned to its [1 1 0] direction and (b) the $(FeCr)_3O_4$ spinel layer right underneath the Fe_3O_4 layer; (a) taken from magnetite layer and (b) taken from spinel layer close to magnetite/spinel layer interface.
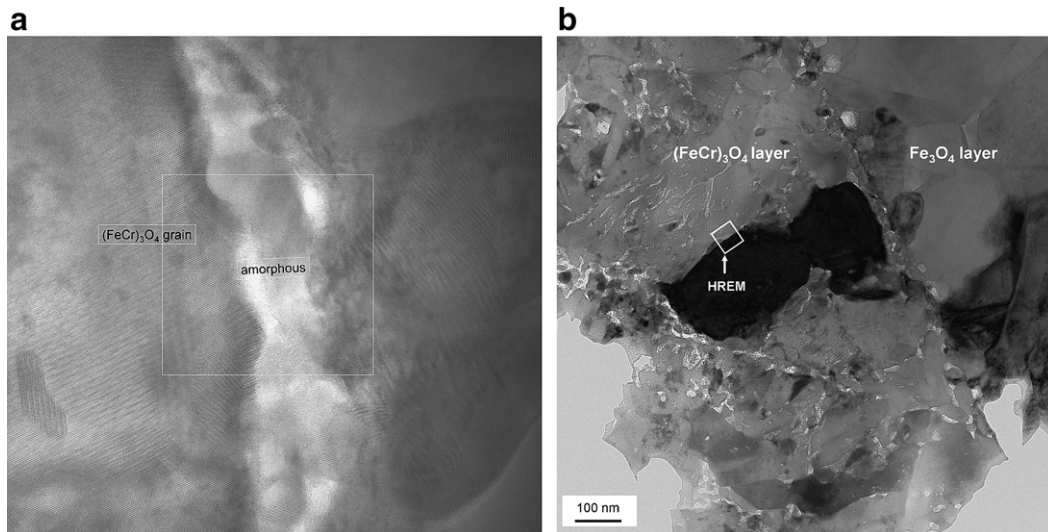

Fig. 6. High resolution electron microscopy (HREM) image (a) showing the nanodomain taken in the region between two $(FeCr)_3O_4$ spinel grains marked by the square in (b).

patterns shown in Fig. 8(b) is consistent with that of the spinel phase, indicating that the crystalline nanoprecipitates are in fact the spinel phase. The other type of the precipitates, which are of cubic morphology and with sizes ranging from several tens nanometers to about 100 nm were identified to be amorphous.

The morphology of the grains and the grain boundaries in the internal oxidation layer of the ODS steel is shown in Fig. 9. This TEM observation indicates three different regions with clearly different features. These three regions include the intragranular region marked O1, the intergranular ribbon region marked O2, and the phase in the region of

the triple point between the grains of the base steel marked O3. These three regions were investigated by EDS and the associated X-ray spectra and the results are presented in Fig. 10(a)–(c), respectively. O1 represents grains with a large amount of secondary phase precipitates, and dominate the internal oxidation layer. EDS analysis of this region shown in Fig. 10(a) indicates a 10:1 of Fe to Cr weight ratio, which approximately represents the base composition of the steel, and the structure is identified as ferrite by the select area diffraction pattern shown in Fig. 8. A relatively small yttrium signal may also be seen in this region by amplifying the signal. EDS of the region marked O2 in Fig. 10(b)
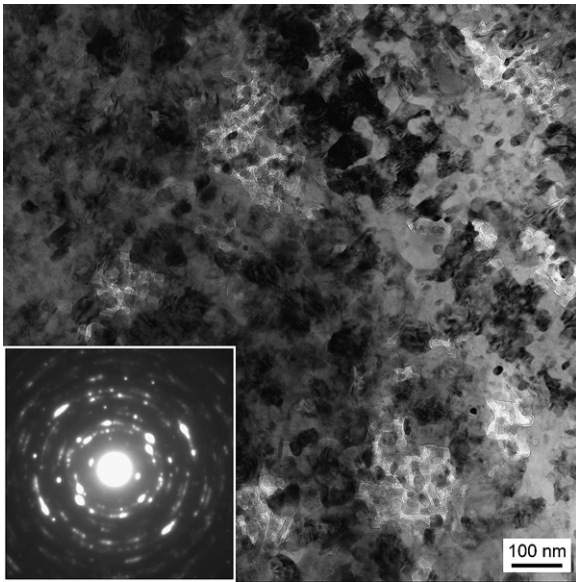
Fig. 7. TEM image showing the morphology of the grain structure in the interior of the (FeCr)$_3$O$_4$ layer of the exposed 9Cr ODS steel.
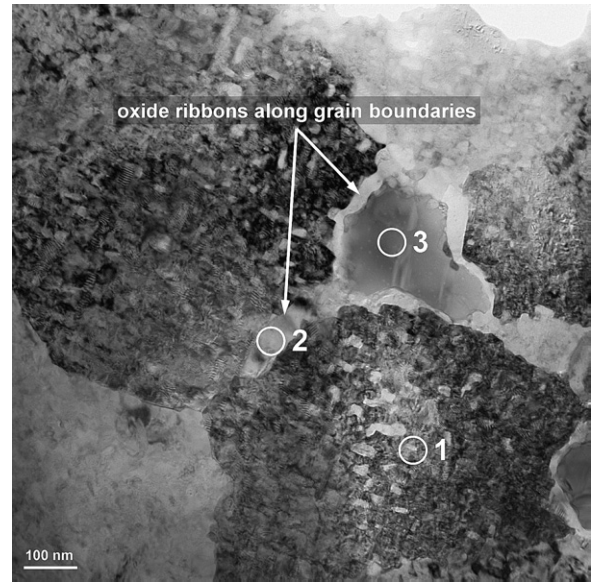

Fig. 9. TEM image showing the morphology of the grains and grain boundaries in the internal oxidation layer formed in the oxidized 9Cr ODS steel.

shows a significant enrichment of Cr. The characteristic peak of yttrium is seen in the X-ray spectrum, indicating yttrium has segregated to the oxide/metal grain boundaries and these Cr-rich oxide ribbons.

The region marked by O3 is an oxide grain that nucleated and grew at the triple point of the substrate ferritic grains. As shown in Fig. 10(c), this region is also enriched in Cr, but not to the extent
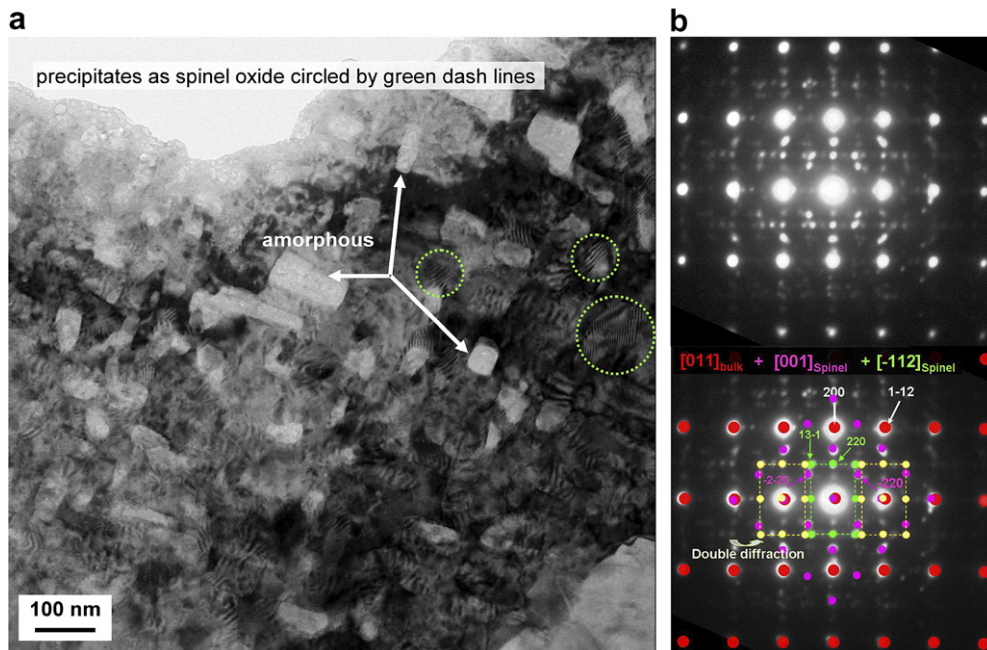

Fig. 8. (a) TEM image showing a grain in the internal oxidation layer of the oxidized 9Cr ODS steel. Arrows indicate precipitates that do not show any fringe pattern, the green circles indicate Moiré fringe domains caused by precipitates that are not aligned with the zone axis. (b) The corresponding selected area electron diffraction patterns taken from the [011] zone axis.
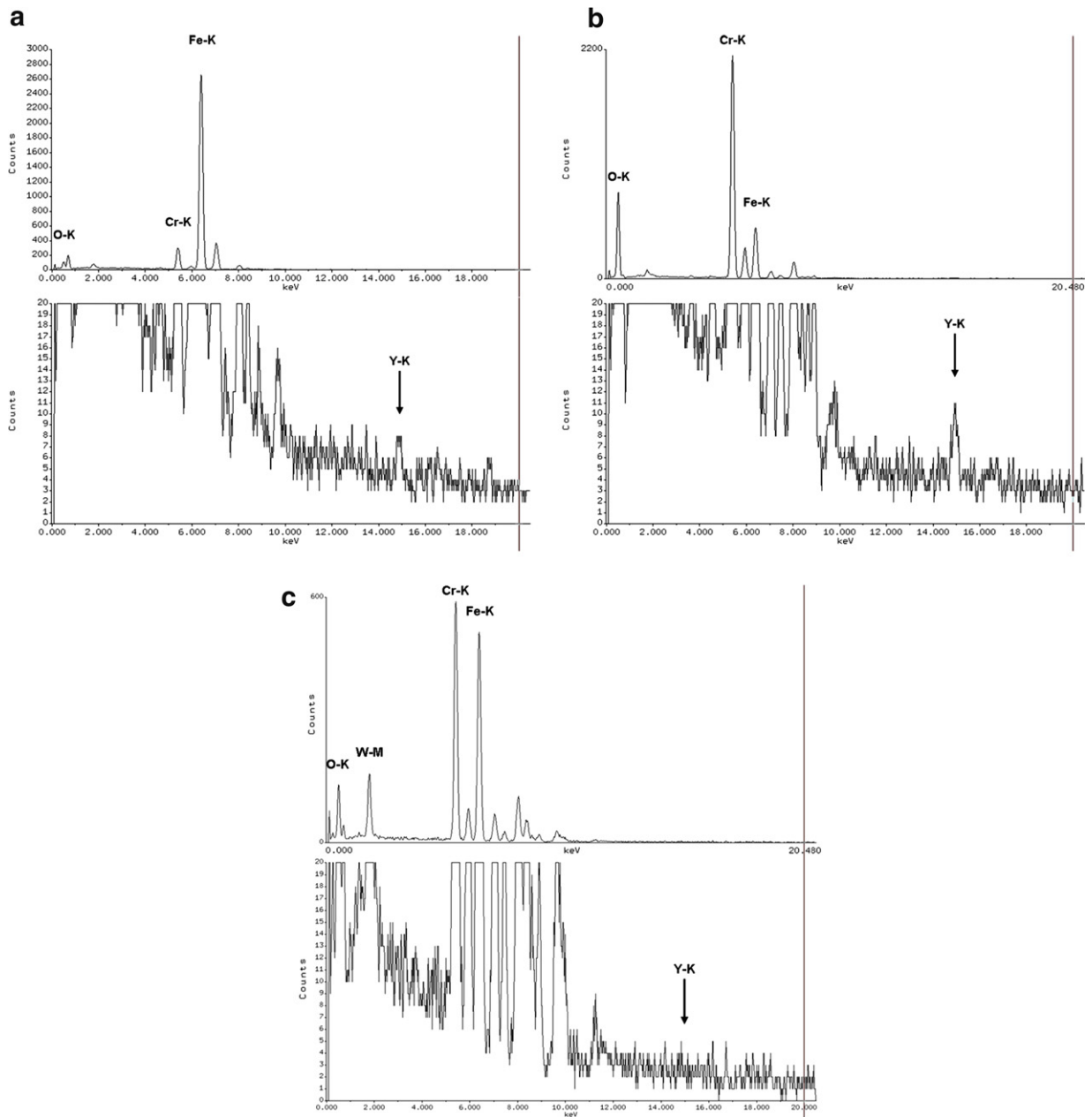
Fig. 10. EDS analyses of x-ray spectra from the different regions in the internal oxidation layer of the oxidized 9Cr ODS steel. (a) O1: intragranular region. (b) O2: ribbon along grain boundary. (c) O3: newly grown oxide grain at the triple-point of the ferritic grains.

as region O2. Furthermore, no characteristic peak related to yttrium could be detected in region O3, indicating yttrium did not enter this newly grown oxide grain during the oxidation process.

4. Discussion

In general, parabolic growth rate behavior for high temperature oxidation implies that oxide growth occurs by diffusion transport, with anion and/or cation transport through the scale as the predominant rate-controlling step. The process of scale growth is therefore in a steady state, with the rate of scale thickening and the density of the scale remaining nearly constant and proportional to the flux of reacting ions. In the 500 °C supercritical water environment, most ferritic steels such as 9Cr NF616 steel (in Fig. 3) and T91 [10] and 12Cr steel

HCM12A [11] follow this type of parabolic oxidation behavior. For the p-type metal-deficit oxide that usually forms on Fe–Cr based alloys, metallic cations are provided at the oxide/alloy interface and migrate through the scale by exchange with the dominant oxide defect, and migration of cations through the oxide layer becomes the rate controlling step [12,13]. For example, magnetite (Fe_3O_4) is a p-type metal deficit oxide semiconductor with cation vacancies ($Fe_{3-y}O_4$) and the self-diffusion coefficient of iron in magnetite is far greater than that of oxygen.

In the present case, the scale of the 9Cr ODS shown in Fig. 1(a) indicates a porous magnetite layer with microcracks. Additionally, numerous pores and voids also appeared in the $(FeCr)_3O_4$ layer. The size of the pores in the spinel dramatically increased as one proceeds inwards away from magnetite/spinel interface, approaching micron scale size in the region close to $(FeCr)_3O_4$ layer/internal oxidation layer interface. Such morphology is confirmed by the TEM observation (Fig. 7) in which the interconnected pores were identified in the $(FeCr)_3O_4$ layer. On the other hand, few voids and pores could be found in the Fe_3O_4 layer of the NF616 scale. The results are supported by Fig. 3, in which the scale of NF616 showed a higher average density compared with that formed on 9Cr ODS. This indicates that a more protective oxide film was formed on the NF616 rather than on the 9Cr ODS. In other words, this suggests that for the 9Cr ODS steel the scale microstructure is not the predominant factor that can be attributed to the noticeable reduction of its oxidation rate.

In the internal oxidation layer of the oxidized 9Cr ODS steel, numerous spinel precipitates and amorphous oxides were seen to nucleate and grow as sub-grain particles in the interior of the ferritic grains. Correspondingly, the oxide grains in the $(FeCr)_3O_4$ layer are mainly composed of a large amount of nanometer sized sub-grains (Fig. 7). Since both microstructures are quite similar, we suggest that the formation of the $(FeCr)_3O_4$ grains might be traced back to the microstructural developments in the previous ferritic grains in internal oxidation layer.

As shown in Fig. 9 and Fig. 10(b), oxide ribbons developed along the grain boundaries of the steel in the internal oxidation layer and are identified as Cr rich oxides, suggesting that Cr preferentially migrated to the ferritic grain boundaries and was primarily oxidized during the exposure. Some

yttrium has also segregated to the Cr-dominant oxide ribbons. Attempts were made to identify the yttrium-containing phase in the oxide ribbons, but a positive identification could not be made because the area of yttrium-rich oxide was exceedingly small and no crystals of a suitable orientation were identified. Based upon the results of Caudron et al. [14] who observed $YFeO_3$ in yttrium ion implanted iron and Przybylski et al. [15] who observed that $YCrO_3$ was formed in yttrium implanted Co–45Cr, it is speculated that the phase formed in the yttrium contained oxide may be YMO_3 (M: Fe or/and Cr). Thermodynamic data for the formation of $YFeO_3$ in Fe–Y–O system at elevated temperatures were studied by Piekarczyk et al. [16]. The results indicate that the formation of $YFeO_3$ from metallic iron, yttrium oxide and oxygen is thermodynamically possible, especially in environments at relatively low temperatures and low oxygen content. This suggestion is also supported by the investigation carried out by Zeng et al. [17] who studied the oxidation behavior of Fe–Y alloys containing 2–5 at.%Y at 600–800 °C in air and reported the existence of $YFeO_3$ phase in the inner mixed oxide layer which significantly enhanced inward oxygen diffusion and decreased outward iron diffusion. Also as presented in Fig. 10(c), no yttrium was detected in the grain located at the triple point of ferritic grains, indicating yttrium was trapped in the initially formed Cr rich oxide ribbons.

Most authors conclude that alloys containing yttrium are oxidized by inward diffusion of anions at elevated temperatures [5,6,14,15]. Based on our initial experiments, it appears that inward oxygen diffusion plays a significant role in the oxidation of 9Cr ODS steel in 500 °C supercritical water environment. On the basis of this hypothesis, the oxidation behavior of the 9Cr ODS steel in supercritical water could be substantially understood. The 9Cr ODS steel with fine grains provides a large amount of short-circuit transport paths for both anion and cation diffusion. In the initial stages, the Y–Cr-rich oxides preferentially nucleate and grow as an interconnected network at the grain boundaries of the base steel, owing to the high oxygen affinities of chromium and yttrium compared with that of iron. These grain boundaries may act as the major path for cation diffusion for subsequent oxidation process. The formation of these ribbons reduced the cation flux at these regions, while not decreasing the inward oxygen diffusion, consistent with the work of Zeng [16]. Therefore, the species that

diffused at the highest rate in the system changed from cations to anions, and the location of the reaction to form new oxide changed from the scale/oxygen interface to the steel/scale interface.

As a result, the overall corrosion rate of the 9Cr ODS decreased and the scales formed on this steel are thinner than those observed on NF616 steel (as shown in Fig. 3). Relative high oxygen flux along the grain boundaries created an internal oxidation zone deep into the steel. To the extent the high oxygen concentration gradient between oxide and substrate also enhanced the diffusion of oxygen in the steel and resulted in the formation of more oxide precipitation in the ferritic matrix. Because of the reduced Fe diffusion from the base metal, the Fe necessary to form additional magnetite in the outer layer comes from the spinel layer. The consumption of iron cations is not balanced by the outward flux of reacting iron ions at the oxide/metal interface. To maintain electroneutrality, more vacancies have to be induced and such defects will migrate and coalesce to become pores in the spinel layer. The additional porosity provides a possible explanation for the decreasing density of the oxide layer at longer exposure times as observed in this study for the 9Cr ODS steel.

5. Conclusion

In terms of weight gain, the 9Cr ODS ferritic steel showed an improved oxidation resistance compared to a conventional 9Cr ferritic steel NF616 with a similar major element composition, when exposed to supercritical water at 500 °C with 25 ppb dissolved oxygen. In contrast to the NF616 steel, the ODS steel exhibited a more porous oxide structure and a substantially deeper internal oxidation zone.

TEM investigation with EDS analysis revealed that yttrium preferentially segregated to oxide ribbons that formed along the oxide/metal grain boundary regions in the internal oxidation layer. The formation of these ribbons likely reduced the cation flux at these regions, while not significantly affecting inward oxygen diffusion.

Primary oxide growth occurred in the internal oxidation layer and was controlled by slow oxygen diffusion. This differs from ferritic–martensitic steels with similar Cr contents where growth is primarily due to faster iron cation diffusion that expands the magnetite and spinel layers.

The depletion of iron cations in the $(FeCr)_3O_4$ layer resulted in the formation of vacancies which eventually coalesced into pores and thereby caused the gradual decrease of the scale densities with the increase of the exposure time.

References

[1] J. Stringer, Mater. Sci. Eng. A 120 (1989) 129.
[2] Yun Chen, Kumar Sridharan, Todd R. Allen, Corrosion of 9Cr Dispersion Strengthened Steel in Supercritical Water Environment, in: Proc. of 2006 ANS Annual Meeting, Reno, submitted for publication.
[3] P.Y. Hou, J. Stringer, Mater. Sci. Eng. A 202 (1995) 1.
[4] M.K. Miller, D.T. Hoelzer, E.A. Kenik, K.F. Russell, Intermetallics 13 (2005) 387.
[5] C.M. Cotell, G.J. Yurek, R.J. Hussey, D.F. Mitchell, M.J. Graham, Oxidation Met. 34 (1990) 173.
[6] T.A. Ramanarayanan, R. Ayer, R. Petkovic-Luton, D.P. Leta, Oxidation Met. 29 (1988) 445.
[7] J.K. Tien, F.S. Pettit, Metall. Trans. 3 (6) (1972) 1587.
[8] S. Ohtuska, S. Ukai, M. Fujiwara, T. Kaito, T. Narita, Mater. Trans. 46 (3) (2005) 1.
[9] K. Sridharan, A. Zillmer, J.R. Licht, T.R. Allen, M.H. Anderson, L. Tan, Corrosion Behavior of Candidate Alloys for Supercritical Water Reactors, in: Proc. of ICAPP 04, Pittsburgh, PA, 2004. p. 537.
[10] Y. Chen, K. Sridharan, T. Allen, Corros. Sci. 48 (9) (2006) 2843.
[11] L. Tan, Y. Yang, T.R. Allen, Corros. Sci., in press.
[12] P.R. Roberge, Handbook of Corrosion Engineering, McGraw-Hill, New York, 1999, p. 234.
[13] D.A. Jones, Principles and Prevention of Corrosion, second ed., Prentice-Hall, Upper Saddle River, 1996.
[14] E. Caudron, H. Buscail, Surf. Eng. 16 (2000) 525.
[15] K. Przybylski, A.J. Garratt-Reed, G.J. Yurek, J. Electrochem. Soc. 135 (2) (1988) 511.
[16] W. Piekarczyk, W. Weppner, A. Rabenau, Mater. Res. Bull. 13 (1978) 1077.
[17] C.L. Zeng, F.C. Rizzo, M.J. Monteiro, W.T. Wu, Oxidation Met. 51 (1999) 495.